Available online at www.sciencedirect.com

SciVerse ScienceDirect

Ceramics International 39 (2013) 5113–5124

CERAMICS INTERNATIONAL

www.elsevier.com/locate/ceramint

Influence of original powders on the microstructure and properties of thermal barrier coatings deposited by supersonic atmospheric plasma spraying, Part I: Microstructure

Y. Bai[a,b], J.J. Tang[a], Y.M. Qu[a], S.Q. Ma[a], C.H. Ding[c], J.F. Yang[a], L. Yu[b], Z.H. Han[a,*]

[a]State Key Laboratory for Mechanical Behavior of Materials, Xi'an Jiaotong University, Xi'an 710049, PR China
[b]School of Mechanical Engineering, Xi'an Jiaotong University, Xi'an 710049, PR China
[c]State Key Laboratory for Strength and Vibration of Mechanical Structures, Xi'an Jiaotong University, Xi'an 710049, PR China

Received 7 September 2012; received in revised form 2 December 2012; accepted 2 December 2012
Available online 10 December 2012

Abstract

In this work, two types of yttria-stabilised zirconia (YSZ) powders, a microsized powder and a reconstituted nanostructured powder, were used as the original feedstock for depositing thermal barrier coatings (TBCs) using a high-efficiency supersonic atmospheric plasma spraying (SAPS) system. The effect of the original powder on the coating microstructure was studied by scanning electron microscopy (SEM) and high-resolution transmission electron microscopy (HRTEM). The results indicated that the microsized powder was fully melted in the plasma jet and that the as-sprayed conventional coating (named MC) was composed of regular-shaped tetragonal ZrO_2 with grain size of 200–500 nm. However, the cross-section morphology of the water-quenched powders revealed that the reconstituted nanostructured powder was partially melted during plasma spraying and that the as-sprayed nanostructured coating (named NC) exhibited a multi-modal microstructure that mainly consisted of unmelted nanoparticles (30–50 nm) and nanograins (60–110 nm), with the latter being the main microstructure of the coating. One visible polycrystalline region consisting of 10 nm grains was also found in NC. In addition, due to the full melting of the microsized powder in the plasma jet, MC exhibited a lower porosity and higher microhardness and Weibull modulus compared with those of NC. In the following paper (Part II), the thermo-mechanical properties, such as thermal shock resistance, oxidation resistance and thermal insulation performance, of the above two coating types will be further studied.

Keywords: B. Grain size; Supersonic atmospheric plasma spraying; Thermal barrier coatings; Nanostructured coating

1. Introduction

Yttria-stabilised zirconia (YSZ)-based thermal barrier coatings (TBCs), deposited by atmospheric plasma spraying (APS) or electron-beam physical-vapour deposition (EB-PVD), have been employed for many years to protect the hot section components of gas turbine engines against high-temperature environments[1,2]. Recently, plasma-sprayed nanostructured ceramic coatings have received significant attention in academic research and industry applications due to the possibility of obtaining greatly improved properties relative to conventional coarse-grained coatings [3]. Previous investigations illustrated that the nanostructured YSZ coatings exhibited a higher thermal cycling life, lower thermal conductivity and higher oxidation resistance with respect to microstructured conventional coatings. For example, Liang et al. found that the number of thermal shock cycles to failure of the nanostructured YSZ coating was approximately two to three times that of conventional YSZ coating from 1000 to 1300 °C [4]. According to Zhou et al., the thermal diffusivity of the as-sprayed nanostructured YSZ coating was $2.15–2.75 \times 10^{-3}$ cm^2/s from room temperature to 800 °C, whereas the corresponding thermal diffusivity of conventional YSZ coating was $2.35–2.96 \times 10^{-3}$ cm^2/s [5]. In addition, Wang et al. showed that the weight gains of the nanostructured and conventional coatings at 1200 °C

*Corresponding author. Tel.: +86 29 82668614; fax: +86 29 82663453.
E-mail address: zhhan@mail.xjtu.edu.cn (Z.H. Han).

0272-8842/$ - see front matter © 2012 Elsevier Ltd and Techna Group S.r.l. All rights reserved.
http://dx.doi.org/10.1016/j.ceramint.2012.12.007

for 110 h were 2.885 and 3.222 mg/mm^2, respectively [6]. The significant improvements in the thermal and mechanical properties of the nanostructured coatings may be attributed to the presence of micro-pores, decreased grain size, increased splat boundary strength and decreased splat interfacial stress [3–8].

During the plasma spraying process, the starting feedstock powders are injected into the plasma jet, where are melted and accelerated against the substrate to form a compact coating. Consequently, the structure of the as-sprayed coating is strongly dependent on the feedstock powder. Agglomerated and sintered powders or fused and crushed powders are widely used to deposit TBCs. In the former, powders are often spray-dried to agglomerate many smaller powders into larger ones and then sintered to increase the powder density [9–11]. Individual nanosized powder particles cannot be carried in a moving gas stream and deposited on a substrate due to their low mass and flowability. Therefore, nanostructured powders are generally agglomerated by spray-drying and then partially sintered into microscopic particles [12]. As-sintered bulk materials that are consequently crushed into powders are referred to as fused and crushed powders. Powders of this type are often utilised as the feedstock for depositing so-called conventional plasma sprayed YSZ coatings [3–5].

To date, great efforts have been made to understand the microstructure and property differences between nanostructured and conventional YSZ coatings. However, the conventional coating usually originates from conventional feedstock, which is usually polyhedral, irregular and angular because it is obtained by sintering and crushing in the actual process. These properties will affect its flowability in the plasma spray process and decrease the coating deposition efficiency [13,14]. In fact, as previously stated, the microstructures and properties of thermal sprayed coatings are significantly affected by feedstock characteristics, such as morphology, size distribution and flowability, and the spraying process conditions. All of these factors have a strong influence on the heat and momentum transfer between the powder and plasma jet. The conventional YSZ coatings deposited by atmospheric plasma spraying using the fused and crushed powders as feedstock usually have more inter-splat pores and a lower bonding strength compared with nanostructured coatings [4,6,14]. Therefore, it is important to determine whether the conventional YSZ coating will exhibit a porous structure and low thermo-mechanical properties if the spray process and feedstock powder are improved.

Recently, an advanced high-efficiency supersonic plasma spraying system (SAPS) has been successfully developed by the National Key Laboratory for Remanufacturing (Beijing, China) for the deposition of ceramic and metallic coatings with good performance [15–17]. Due to the structural optimisation of the spray gun and internal powder injection, the in-flight particles acquire greater energy and momentum in the SAPS system. Our previously results showed that the SAPS coating had a finer microstructure and higher bonding strength than the conventional APS-YSZ coating [18]. The SAPS method is likely to be used to deposit high-performance TBCs at lower cost. However, little information is available about the effect of feedstock powders on the structure and properties of SAPS coatings at present.

Based on the above background, two types of yttria-stabilised zirconia (YSZ) powders, an agglomerated micro-scale powder and a reconstituted nanostructured powder, were chosen as the original feedstock powders for depositing thermal barrier coatings (TBCs) using the SAPS system in the present work. The objectives of this and subsequent works include: (1) studying the effect of the original powders on the microstructure of SAPS coatings and (2) evaluating the difference in thermo-mechanical properties between the nanostructured and conventional SAPS coatings to provide a deeper understanding of the SAPS-TBCs.

2. Experimental procedure

2.1. Materials

The substrate, GH3030 nickel-based superalloy with dimensions of $\Phi 20\,\text{mm} \times 10\,\text{mm}$, was ultrasonically cleaned and then grit-blasted with alumina powder to increase the adherence capability between the bond coat and substrate. The surface roughness (R_a) of grit-blasted substrate was 6.25 ± 0.38 μm measured with a profilometer (TR 240, Beijing Time Group, Beijing, China). A commercially available CoNiCrAlY powder (AMDRY 995 M, Sulzer Metco Inc. Westbury, NY, USA) with a nominal composition of Ni-32, Cr-21, Al-8, Y-0.4 Co-balance (wt%) was used for spraying the TBC bond coat. Two spray-dried and sintered ZrO_2–8 wt% Y_2O_3 powders were used as the original feedstock for depositing the top ceramic coat. The morphology, internal structure and particle size distribution of the two powders are provided in Figs. 1 and 2. The first feedstock exhibited a near-perfect spherical morphology with a particle size of 25–90 μm; the small particles inside the feedstock were well compacted, with a grain size of 200–700 nm. The as-sprayed coating using this type of powder as the feedstock was named "MC". The second feedstock exhibited a sintered shell with a grain size of 30–50 nm inside the shell. The particle size of the second feedstock varied from 40 to 110 μm. The coating produced from the second powder was named "NC". Laser particle size analysis (Model Rise-2008, Jinan Rise Science & Technology Co., Ltd., Jinan, China) showed that the median particle sizes (D_{50}) of the MC and NC powders were 45.2 and 67.5 μm, respectively.

2.2. Plasma spraying process

The thermal barrier coatings, composed of a bond CoNiCrAlY coat and a top YSZ coat, were deposited by a high-efficiency supersonic atmospheric plasma spraying

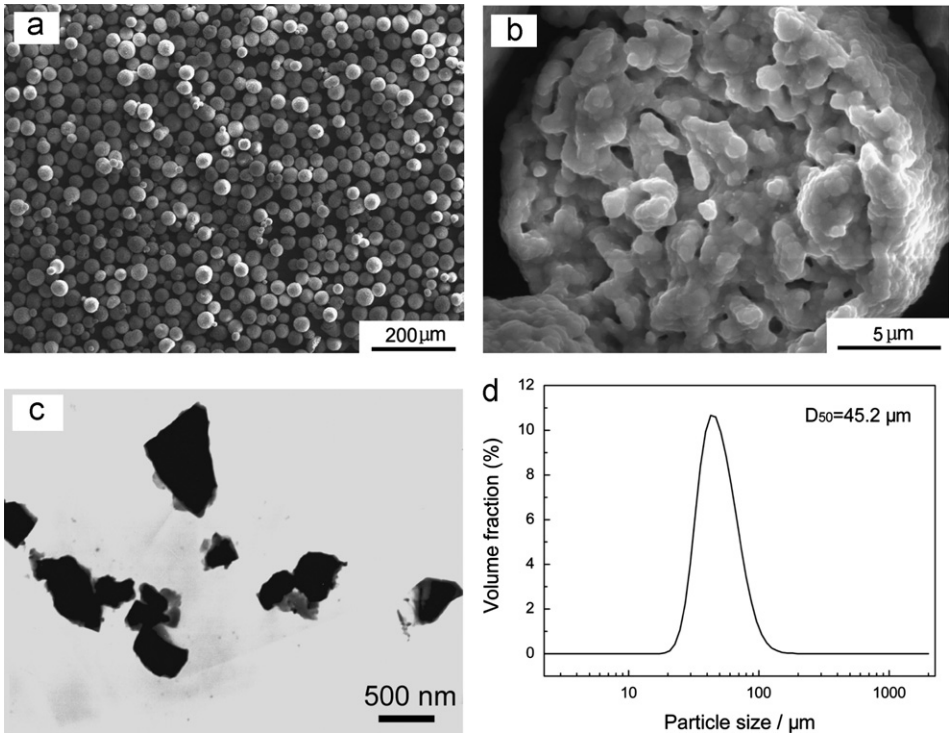

Fig. 1. Morphology, structure and particle size distribution of original microsized powder: (a) morphology of particles, (b) cross-section of single particle, (c) TEM image, (d) particle size distribution.

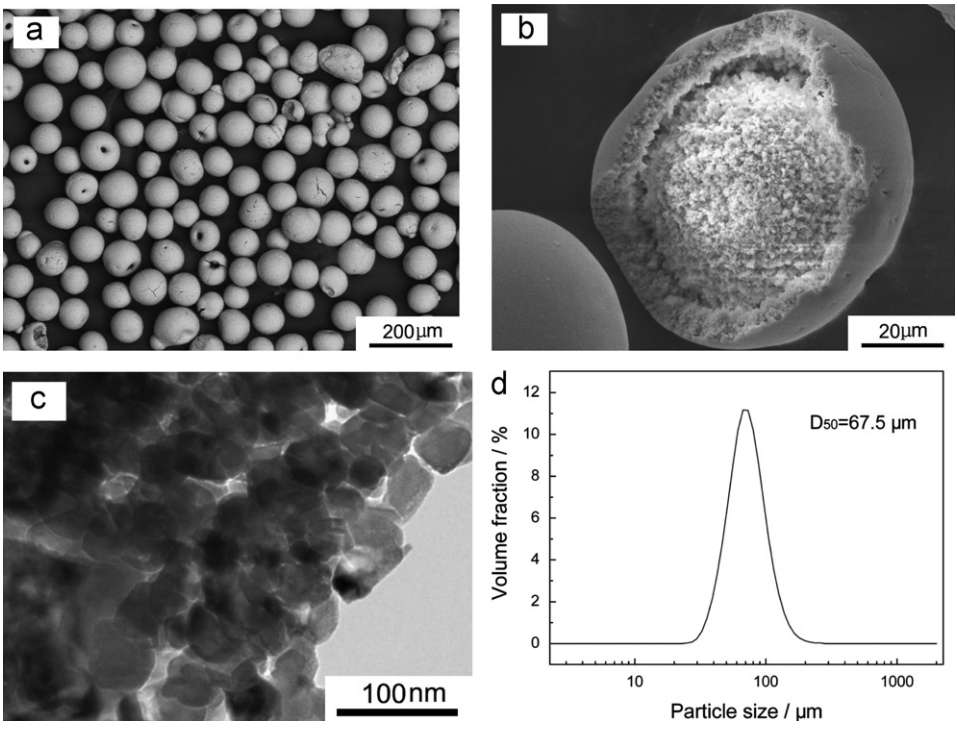

Fig. 2. Morphology, structure and particle size distribution of original nanostructured powder: (a) morphology of particles, (b) cross-section of single particle, (c) TEM image, (d) particle size distribution.

(SAPS) system. The spray parameters are presented in Table 1. During the spraying process, the substrate was cooled by compressed air and the temperature of substrate was held at approximately 100–200 °C, as monitored by a NiCr/NiSi thermocouple attached to the back of the substrate.

Table 1
Spray parameters for CoNiCrAlY and YSZ powders.

Parameters	CoNiCrAlY	YSZ
Gun nozzle inner diameter (mm)	6	6
Powder injection port inlet diameter (mm)	2	2
Current (A)	363	405
Voltage (V)	124	160
Primary gas Ar (slpm)	65	60
Second gas H_2 (slpm)	8	17
Carrier argon gas flow rate (slpm)	8	7.5
Gun traverse speed (mm/s)	800	800
Powder feed rate (g/min)	40	40
Spray distance (mm)	100	100

* It was noted that the powder injection port was inside the nozzle and positioned at a distance of 12 mm from the nozzle outlet.

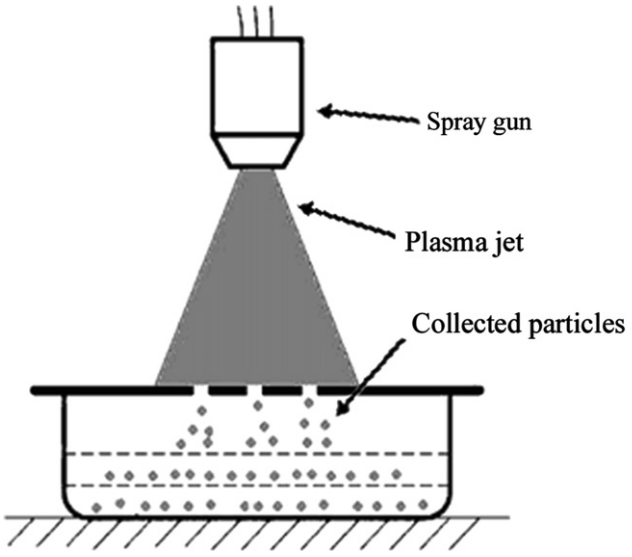

Fig. 3. Schematic of sprayed particles collector.

2.3. Particle in-flight properties

During spraying, a commercially available Spray Watch 2i system (Osier, Finland) was used to monitor the velocity and surface temperature of in-flight particles for each set of operating conditions. In this system, velocity and surface temperature of individual particle were measured by time-of-flight method and two-colour pyrometry, respectively. The measurement was performed at State Key Laboratory for Mechanical Behaviour of Materials (Xi'an Jiaotong University, Xi'an, China). Approximately 2000 particles were independently detected for each measurement, and the final value was the average of five measurements. In addition, the in-flight particles were collected using a set-up described in [19] and shown in Fig. 3.

2.4. Specimen characterisation

The coating was characterised by X-ray diffraction (XRD, D/MAX-2400X, Rigaku, Japan) using Cu K_α radiation. The microstructure of the as-sprayed coating was observed by scanning electron microscopy (SEM; VEGAII XMU, Tescan, Czech Republic) and high-resolution transmission electron microscopy (HRTEM; JSM-6700F, JEOL, Japan). After the substrate was removed from the as-sprayed coating by dissolution in hydrochloric acid, a plane-view specimen for TEM analysis was prepared by mechanical grinding, polishing and dimpling, followed by Ar-ion milling using a Gatan 691 precision ion polishing system (Gatan Inc., USA). The HRTEM was equipped with an X-twin objective lens with a coefficient of spherical aberration $C_s = 1.0$ mm (point-to-point resolution of 0.23 nm) and operated at a 200 kV accelerating voltage.

The porosity of the coatings was estimated by the Archimedean (water displacement) method and quantitative image analysis (IA) using a picture analysis system in scanning electron microscopy. In the Archimedean method, the top YSZ coat was first separated from the metallic substrate by submerging the samples in 40% hydrochloric acid until the metallic bond coat was dissolved. Next, the free-standing YSZ top coat was cleaned and dried. Before measurement, the samples were boiled in distilled water for 2 h to facilitate pore penetration. A detailed description of the Archimedean technique used to determine the coating porosity was available in the literature [20]. In the image analysis, a series of SEM images with a 1000× magnification were obtained for individual specimens to obtain a representative porosity value. The image resolution was 600 dpi, and the minimum area of the detectable voids was approximately 0.1 μm^2.

2.5. Microhardness and Weibull analysis

The coating microhardness was measured by a microhardness tester (MicroMet 3 microhardness tester, Buehler Ltd., USA). The polished cross section of the coating was measured 30 times at different areas with a load of 2.94 N and a holding time of 10 s while maintaining a distance between consecutive indentations at least five times greater than the diagonal length of indentation. The microhardness data scatter was treated using Weibull statistical analysis. The two-parameter Weibull distribution function was utilised and given as [21–23]

$$F(x) = 1 - \exp\left[-\left(\frac{x}{x_0}\right)\right]^m \quad (1)$$

where $F(x)$ is the cumulative density function of probability; x is the microhardness data; x_0 is the scale factor, which gives 63.2% of the cumulative density; and m is the Weibull modulus. The Weibull modulus reflects the data scatter within the distribution. The Weibull plot is the most common and easiest technique for obtaining the Weibull modulus. A Weibull plot can be drawn by rearranging Eq. (1) and taking natural logarithms twice. Thus, x_0 and m can be

determined by fitting the following equation:

$$\mathrm{In}\left\{\mathrm{In}\left[\frac{1}{1-F(x)}\right]\right\} = m[\mathrm{In}(x)-\mathrm{In}(x_0)] \quad (2)$$

The mean value of $F(x)$ is obtained by arranging the data in ascending order and letting [21]

$$F(x) = \frac{i-0.3}{n+0.4} \quad (3)$$

where i is the ith element in an ascending data set and n is the total number of data points.

3. Results and discussion

3.1. Cross-section morphology

Fig. 4 shows the cross-sectional micrographs of as-sprayed MC. As shown in Fig. 4a and b, MC was composed of well-adhered splats and fine inter-lamellar cracks. The columnar structure within the individual splats was visible because rapid nucleation occurred at the cooler surface of the flattened droplet at large under-cooling and the crystals grew rapidly opposite to the heat flow, forming a columnar grain structure. In addition, as observed from Fig. 4c and d, the micro-pores were homogeneously distributed in the coating and no obvious cracks were observed at the interface of the top coat and bond coat, which indicated that the microsized SAPS coating had a denser microstructure and less irregular inter-splat pores and cracks than the previously reported conventional microsized APS coatings [4,6,14]. Fig. 5 shows the SEM images of the as-sprayed NC. As shown in Fig. 5a and b and similarly to MC, a typical lamellar structure with columnar grains was observed because the molten droplets successively impinged and spread on the substrate or previously deposited layers to form continuous splats. However, NC was distinct from MC in that it contained some unmelted feedstock particles loosely distributed between the splats. These unmelted particles retained the initial nanostructure of feedstock, as later confirmed by TEM. Additionally, as shown in Fig. 5c and d, the proportion of unmelted particles (as marked by ellipses) was less than that of the columnar grains formed from the melt. The bonding between the top coat and bond coat was also very good. The image analysis and Archimedean principle indicated that the porosity of MC was approximately 3% and 5%, respectively, whereas the porosity of NC obtained from the above two methods was approximately 5% and 8%, respectively. Therefore, MC was much denser than NC. The higher porosity of NC may be attributed to the unmelted particles, which were loosely distributed in the coating, decreasing the effective bonding surface between splats and leading to the formation of inter-splat pores.

3.2. Melting state of feedstock powder

Fig. 6 shows a cross-section of in-flight particles collected in distilled water. As can be observed, the microsized feedstock powder was fully melted, whereas the

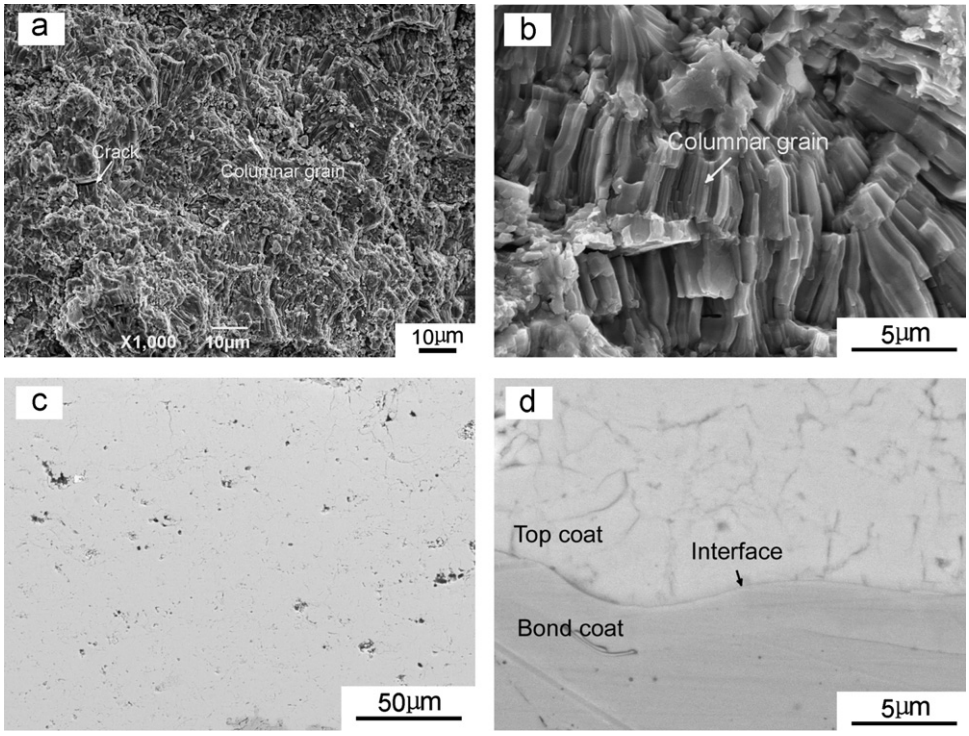

Fig. 4. Cross-sectional micrographs of as-sprayed MC: (a) fractured cross section of the top YSZ coat, (b) a detail view of the columnar grains, (c) polished cross section of the top YSZ coat, (d) interface between top coat and bond coat.

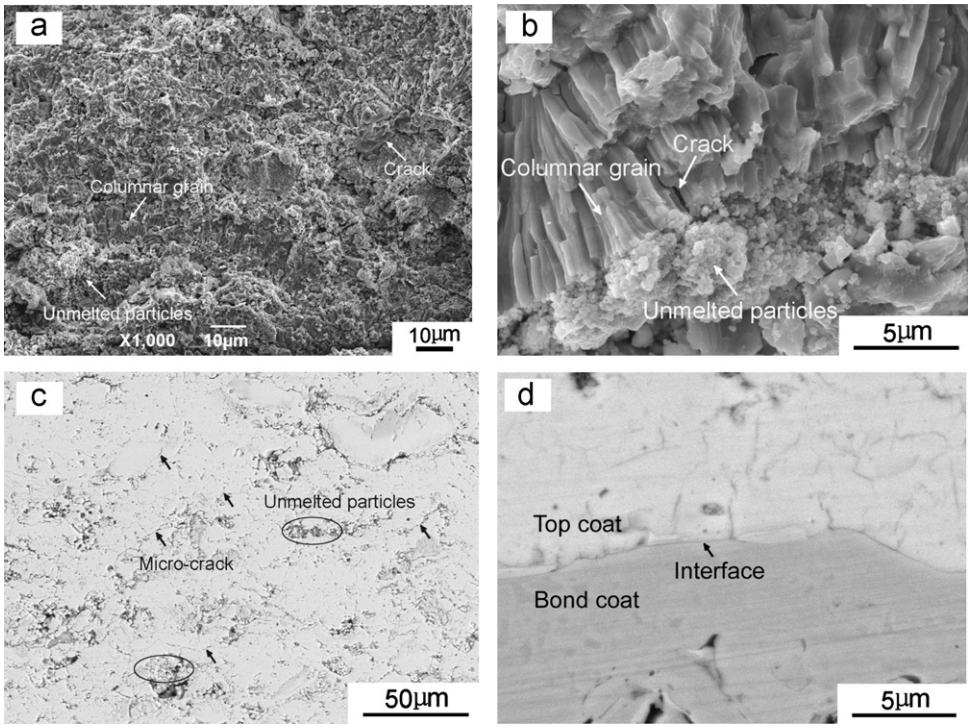

Fig. 5. SEM images of as-sprayed NC: (a) fractured cross-section, (b) a detail view of the columnar grains and unmelted particles, (c) polished cross-section the top YSZ coat of which some fine cracks and unmelted particles were denoted by black arrows and ellipse, respectively, (d) interface between top coat and bond coat.

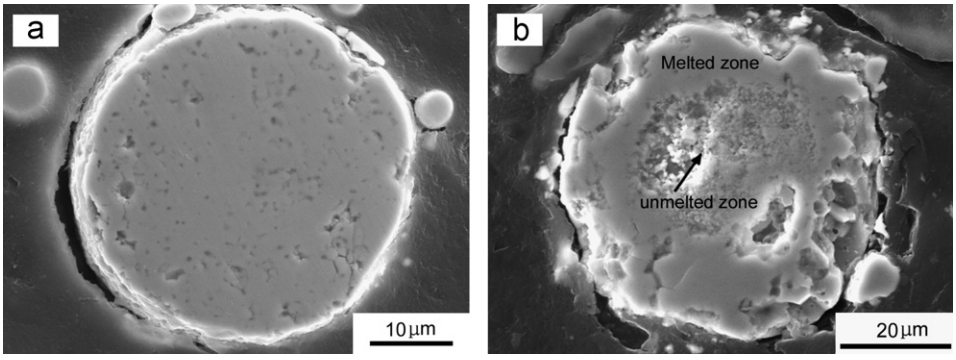

Fig. 6. Cross-sectional micrographs for single particle collected in distilled water: (a) fully melted microsized powder, (b) semi-melted nanostructured powder.

Table 2
Average in-flight velocity and surface temperature of two types of original powders.

	Microsized powder	Reconstituted nanostructured powder
Average velocity (m/s)	430 ± 9	424 ± 11
Average surface temperature (°C)	3200 ± 48	3089 ± 39

reconstituted nanostructured powder was partially melted, retaining some unmelted particles in the central part of the powder. During the plasma spraying, the momentum and energy transfer processes between the plasma and powder are crucial in the melting state of the in-flight particles. The high temperature of the plasma jet can rapidly increase the temperature and melting of the particle after it is injected into the plasma jet. For a YSZ particle, the particle temperature is high at the surface and low at the centre. The average in-flight velocities and surface temperatures of the two original powders are shown in Table 2. Table 2 indicates that the average in-flight velocity and surface

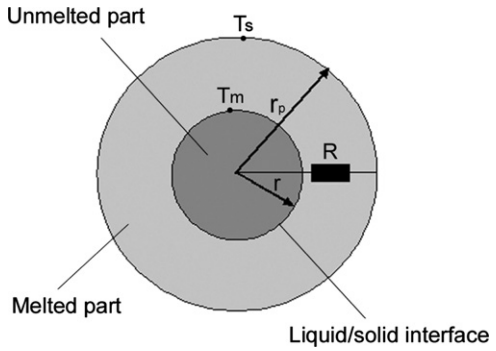

Fig. 7. Schematic of the in-flight particle melting process.

temperature of the microstructured powders in SAPS were 430 m/s and 3200 °C, respectively, which were slightly higher than the corresponding values of 424 m/s and 3089 °C for the nanostructured powder. The surface temperatures of both powders were much higher than the melting point of YSZ (approximately 2700 °C [1]). However, the high temperature at the particle surface could not guarantee complete melting; the melting percentage of the particle depends on its size, thermal conductivity, latent heat, and residence time in the plasma jet. t_{melt}, the total time required for a particle to fully melt, is estimated by thermal resistance analysis. Assuming that the particle is spherical and the heat transfer inside the particle is conduction-dominated, the in-flight particle melting process is illustrated in Fig. 7. According to Xiong et al., the temperature distribution in the unmelted part (solid phase) can be negligible [24]. Therefore, the total heat transferred to the particle melt and solid interface will be balanced with the latent heat absorbed by the particle for melting. This phenomenon is described mathematically as follows:

$$-L \times \frac{dm}{dt} = \frac{T_s - T_m}{R} \tag{4}$$

where L is the latent heat of fusion, m is the mass of the solid phase, t is the residence time of the in-flight particle, T_s is the surface temperature of the in-flight particle and T_m is the melting point of YSZ. R is the thermal resistance by conduction and is given by the following equation [24]:

$$R = \frac{1}{4\pi k}\left(\frac{1}{r} - \frac{1}{r_p}\right) \tag{5}$$

where k is the thermal conductivity of YSZ, r is the radius of the solid phase of the in-flight particle and r_p is the radius of the in-flight particle. Because the in-flight particle is spherical, dm/dt can be given by

$$\frac{dm}{dt} = 4\pi\rho r^2 \frac{dr}{dt} \tag{6}$$

where ρ is the density of the YSZ. Supposing that the morphology of the in-flight particle is constant during melting and substituting Eq. (5) and Eq. (6) into Eq. (4), the following integrated equation can be obtained:

$$\int_{r_p}^{0} r^2\left(\frac{1}{r_p} - \frac{1}{r}\right)dr = \int_0^{t_{melt}} \frac{k(T_s - T_m)}{L\rho}dt \tag{7}$$

Thus, the total melting time is as follows:

$$t_{melt} = \frac{r_p{}^2 L\rho}{6k(T_s - T_m)} \tag{8}$$

As observed from Eq. (8), the total melting time is directly proportional to the square of the particle radius. The median particle sizes (D_{50}) of the microsized and nanostructured powders were 45.2 and 67.5 μm, respectively, and the corresponding values of T_s–T_m were approximately 500 and 389 °C, respectively. According to Eq. (8), the total melting time for the nanostructured powder was approximately three times that of the microsized powder, indicating that the microsized powder was more easily melted than the nanostructured powder. The nanostructured powder was partially melted, and some unmelted particles remained in the central part of the particle. After plasma spraying, these unmelted particles were observed in the as-sprayed NC, as shown in Fig. 5b.

3.3. Grain size distribution

Fig. 8 shows the TEM micrograph and selected area electron diffraction pattern of MC. As observed, the as-sprayed MC was composed of regular-shaped tetragonal ZrO_2 with a grain size of 200–500 nm. Fig. 9 shows the TEM images of the as-sprayed NC. Unlike MC, NC exhibited a multi-modal microstructure and consisted of crystals with grain size of 60–110 nm and unmelted feedstock particles with sizes ranging from 30 to 50 nm, which resembled the morphology of the feedstock powder. MC showed clear grain boundaries, as shown in Fig. 9b, whereas NC had the same grain size distribution as the original feedstock powder, as shown in Fig. 2c and Fig. 9c. The melting state results for the nanostructured YSZ powder during plasma spraying, shown in Fig. 6b, suggested that the nanosized unmelted particles in the coating originated from the central part of the powder and were surrounded by the molten part. Therefore, the crystal, formed from the melt, acted as a binder and retained the coating integrity, as shown in Fig. 5b and c. In addition, a very interesting phenomenon associated with the recrystallisation during the SAPS was observed. As shown in Fig. 9d and e, one visible polycrystalline region consisting of tetragonal ZrO_2 grains with sizes of approximately 10 nm was found in NC. These ultrafine grains were obviously obtained by the crystal nucleation and growth during the solidification of the molten droplets.

The as-sprayed nanostructured YSZ coatings exhibit a multi-modal microstructure, which has been widely discussed in early investigations, and similar observations have also been reported by several authors [13,25–27].

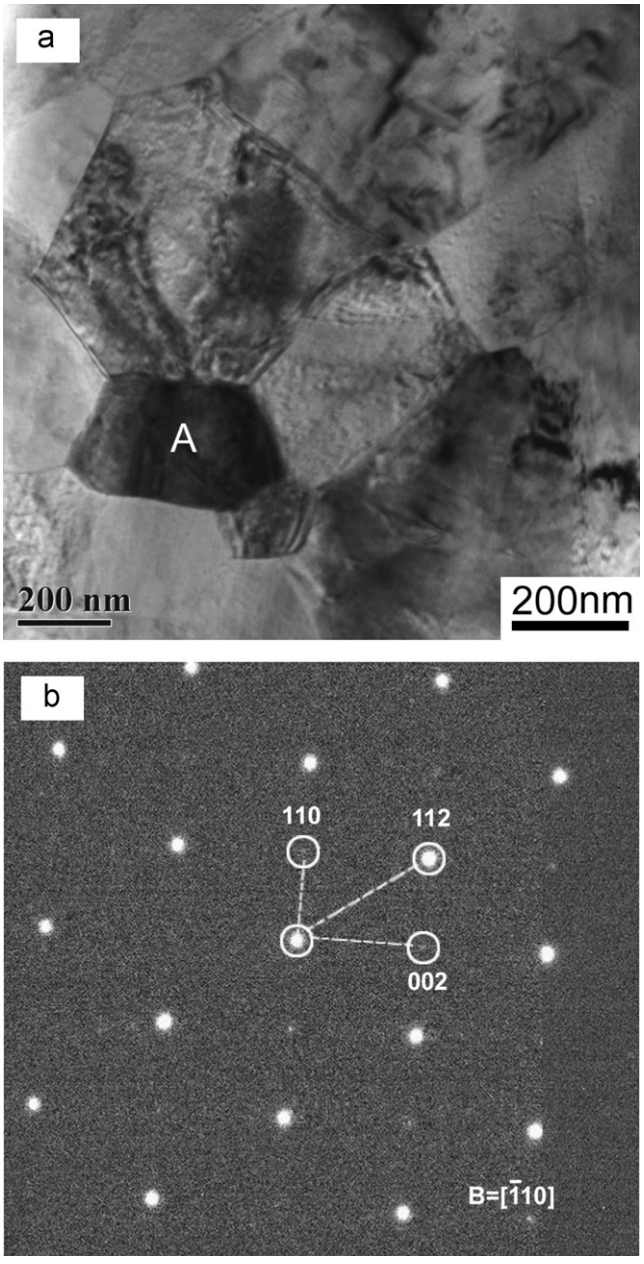

Fig. 8. TEM micrograph of MC: (a) bright field micrograph, (b) selective electron diffraction pattern of grain A.

For plasma spraying, the melting state of particles upon impact will significantly affect the splat morphology and coating structure. It is extremely difficult to produce thermal spray coatings without particle melting. However, if the original particles are fully melted in the plasma jet, the original nanostructural characteristic of the particles may be destroyed [27]. Therefore, preserving the nanostructure of original powder is challenging for depositing the nanosized coating. To overcome this challenge, the temperature of in-flight particles should be carefully controlled such that it is not significantly higher than the melting point of the material to guarantee that some of the initial nanostructure of the original powder is embedded in the coating microstructure. For SAPS, although the surface temperature of the in-flight particles was much higher than the YSZ melting point, the resistance time for particles in the plasma jet was reduced due to the strong improvement in the velocity compared with conventional atmospheric plasma spraying. Hence, the SAPS-YSZ coating retained the nanostructure of the feedstock powder.

3.4. Phase composition of feedstock and corresponding coatings

The X-ray diffraction patterns of two types of YSZ powders and the as-sprayed coatings are shown in Fig. 10. Both of powders were composed of tetragonal, cubic and a small amount of monoclinic phases. In contrast, the ceramic coating only exhibited the non-transformable tetragonal t′ phase of zirconia; no monoclinic phase was found. The metastable tetragonal t′ phase is typical of thermally sprayed zirconia, which is formed due to the quenching of the droplet after impacting on the substrate during plasma spraying [23]. The following formula was used to calculate the amount of monoclinic zirconia in the original powder [25]:

$$Xm = \frac{Im(1\ 1\ 1)+Im(1\ 1\ \bar{1})}{Im(1\ 1\ 1)+Im(1\ 1\ \bar{1})+It(1\ 1\ 1)} \quad (9)$$

where the terms $Im(1\ 1\ 1)$, $Im(11\bar{1})$, and $It(1\ 1\ 1)$ correspond to the peak intensities for $(1\ 1\ 1)$, $(1\ 1\ \bar{1})$ of the monoclinic phase, and $(1\ 1\ 1)$ of the tetragonal phase in the XRD spectra, respectively.

The contents of the monoclinic zirconia phase were approximately 3% and 5% in the microsized and nanosized powders, respectively. However, no monoclinic ZrO_2 peaks were found in either as-sprayed coating, indicating that the monoclinic ZrO_2 in the original powder transformed into the tetragonal ZrO_2 due to the high quenching rate (10^6–10^7 K/s) of the molten droplets [26]. In addition, the mean grain sizes of the tetragonal ZrO_2 phase in the nanostructured powder and as-sprayed NC were estimated using the Scherrer equation [27–29]:

$$B_p(2\theta) = \frac{0.9\lambda}{D\cos\theta} \quad (10)$$

where D is the average dimension of the crystal, B_p (2θ) the broadening of the diffraction line measured at the half-maximum intensity and λ (0.154 nm) and θ denotes the wavelength of the X-rays and the Bragg diffraction angle, respectively. The instrumental broadening is corrected for in the measurement of the peak broadening by comparing the widths at half-maximum intensity of the X-ray reflection between the sample and the single crystalline Si standard. A Gaussian correction is used to remove the instrumental broadening, yielding the true crystal broadening:

$$B_p^2(2\theta) = B_h^2(2\theta) - B_f^2(2\theta) \quad (11)$$

where $B_p(2\theta)$ is the true half-maximum width and $B_h(2\theta)$ and B_f (2θ) are the half-maximum widths of the sample

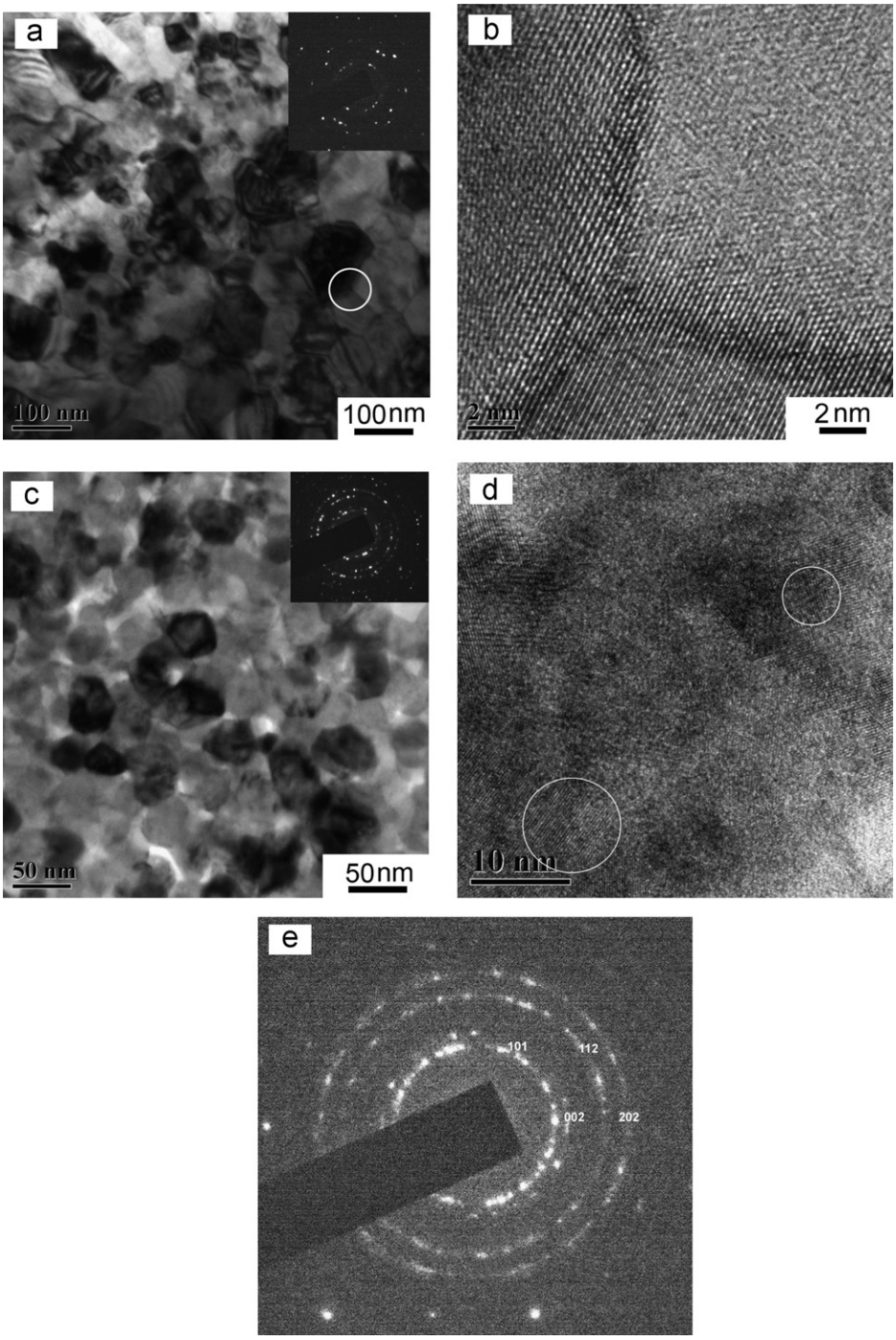

Fig. 9. TEM micrographs of NC: (a) crystals formed from the melt with grain size ranging from 60 to 110 nm, (b) high resolution image of grain boundary of circular region in (a), (c) unmelted particles with grain size of 30–50 nm, (d) ultrafine grains denoted by white circle, (e) electron diffraction pattern of (d).

and the single crystalline Si standard, respectively. The theta value of $2\theta = 30^\circ$ is selected to calculate the crystallite size. Before calculation, the $K\alpha 2$ peak was removed by MDI Jade 5.0 software such that only the $K\alpha 1$ peak widths were used. The calculated average grain sizes of the feedstock powder and as-sprayed coating were approximately 42 and 75 nm, respectively. This result was basically in agreement with that obtained from TEM, as shown in Fig. 9. However, the penetration distance of the X-ray beam into the sample only varies by a few micrometres due to the sample characteristics.

3.5. Microhardness and Weibull analysis

The Vickers hardness at a 2.94 N load for 10 s for NC was $704 \pm 74\ \mathrm{kg/mm^2}$, whereas that for MC was

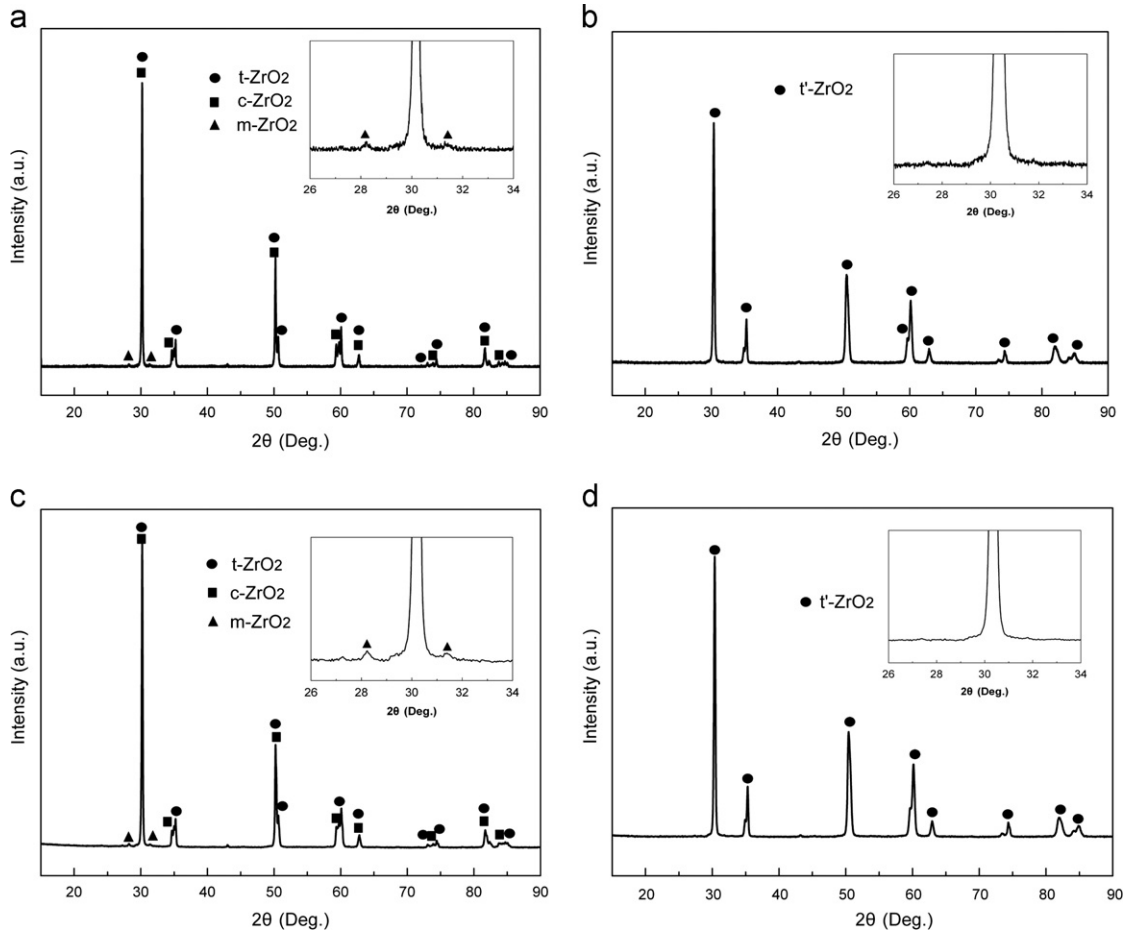

Fig. 10. XRD spectra of original powders and as-sprayed coatings, the inset is the amplification of diffraction peaks in the 2θ ranging from 26° to 34°: (a) original microsized powder, (b) as-sprayed MC, (c) original nanostructured powder, (d) as-sprayed NC.

820 ± 49 kg/mm^2. The lower microhardness of NC may be attributed to the presence of loosely distributed nano unmelted particles and its higher porosity. Fig. 11 shows the probability function of Weibull plots of the Vickers hardness of the two coatings; the Vickers hardness of both coatings involved some scattering due to the nonuniform microstructure of the as-sprayed coatings. The Weibull modulus of MC was 19.5, which was much higher than that of NC. As expected, the larger the M value, the smaller the Vickers hardness of the scattering degree, indicating higher microstructure homogeneity. In addition, as shown in Fig. 11, NC exhibited a bimodal distribution of 14.9 and 5.3. In contrast, MC exhibited a single line for the Weibull modulus. As stated earlier, NC was mainly composed of melted and unmelted particles, which may be considered as two phases. The hardness will be high (low) in regions composed primarily of molten (unmelted) particles. Therefore, the low-slope regions of the Weibull plots reflected microstructural characteristics of the nanostructured feedstock powders, which were molten. On the other hand, the high-slope regions at low hardness values represented the non-molten nanosized particles in the coating microstructure, which was in agreement with the previous reports from Girolamo et al. and Lima et al.

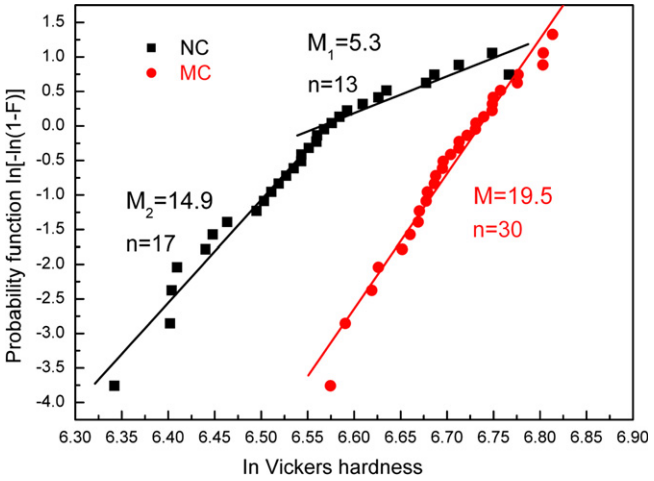

Fig. 11. Welbull distribution of MC and NC.

[26,30]. Additionally, the presence of good interlamellar contact and the absence of macropores and unmelted particles greatly improved the integrity and Weibull modulus of MC relative to NC.

Because the unmelted particles exhibit low hardness, the nanostructured material may lead to TBCs with improved

resistance to residual stress and thermal shock [30]. In addition, the nanostructured coatings could counteract sintering effects due to the presence of a bimodal microstructure exhibiting regions with different sintering rates [31]. Therefore, in the following paper (Part II), the properties, including the thermal shock resistance, thermal insulation performance and oxidation resistance of the microsized and nanosized SAPS coatings, will be further studied.

4. Conclusions

In this study, two types of yttria-stabilised zirconia (YSZ) powders, a microsized powder and a reconstituted nanostructured powder, were used as the original feedstock for depositing thermal barrier coatings (TBCs) by high-efficiency supersonic atmospheric plasma spraying (SAPS). The effect of the original powder on the coating microstructure was studied. The main conclusions are as follows:

(1) The microsized powder was fully melted in the plasma jet, and the as-sprayed SAPS conventional coating (MC) was composed of regular-shaped tetragonal ZrO_2 with a grain size of 200–500 nm.
(2) The nano-agglomerated powder was partially melted during plasma spraying, and the as-sprayed nanostructured SAPS coating (NC) exhibited a multi-modal structure mainly consisting of unmelted nanoparticles (30–50 nm) and nanograins (60–110 nm), with the latter being the main microstructure of the coating. In addition, one visible polycrystalline region consisting of grains with sizes of approximately 10 nm was also found in NC.
(3) The tetragonal, cubic and a small amount of monoclinic phases in both original powders transformed into a non-transformable tetragonal t′ phase after plasma spraying. No monoclinic phase was found in the as-sprayed MC and NC. However, due to the complete melting of the microsized powder in the plasma jet, MC exhibited a lower porosity and higher microhardness and Weibull modulus than NC.
(4) NC exhibited a bimodal Weibull modulus distribution, whereas MC exhibited a single line for the Weibull modulus.

Acknowledgements

This work was supported by the National Basic Research Program (Grant No. 2013CB035701), National Natural Science Foundation for Youth of China (Grant No. 51202187) and Research Fund of Key Laboratory for Advanced Technology in Environmental Protection of Jiangsu Province (Grant No. AE201006). The authors would like to thank Prof. B.J. Ding (Xi'an Jiaotong University, China) and technician Y.M. Qiang (Xi'an Jiaotong University, China) for their suggestions and help.

References

[1] N.P. Padture, M. Gell, E.H. Jordan, Thermal barrier coatings for gas-turbine engine applications, Science 296 (2002) 280–284.
[2] N.P. Padture, K.W. Schlichting, T. Bhatia, A. Ozturk, B. Cetegen, E.H. Jordan, M. Gell, S. Jiang, T.D. Xiao, P.R. Strutt, E. Garcia, P. Miranzo, M.I. Osendi, Towards durable thermal barrier coatings with novel microstructures deposited by solution-precursor plasma spray, Acta Materialia 49 (2001) 2251–2257.
[3] R.S. Lima, B.R. Marple, Thermal spray coatings engineered from nanostructured ceramic agglomerated powders for structural, thermal barrier and biomedical applications: a review, Journal of Thermal Spray Technology 16 (2007) 40–63.
[4] B. Liang, C.X. Ding, Thermal shock resistances of nanostructured and conventional zirconia coatings deposited by atmospheric plasma spraying, Surface and Coatings Technology 197 (2005) 185–192.
[5] C.G. Zhou, N. Wang, Z.B. Wang, S.K. Gong, H.B. Xu, Thermal cycling life and thermal diffusivity of a plasma-sprayed nanostructured thermal barrier coating, Scripta Materialia 51 (2004) 945–948.
[6] W.Q. Wang, C.K. Sha, D.Q. Sun, X.Y. Gu, Microstructural feature, thermal shock resistance and isothermal oxidation resistance of nanostructured zirconia coating, Materials Science and Engineering A 424 (2006) 1–5.
[7] C.G. Zhou, N. Wang, H.B. Xu, Comparison of thermal cycling behavior of plasma-sprayed nanostructured and traditional thermal barrier coatings, Materials Science and Engineering A 452–453 (2007) 569–574.
[8] H. Chen, Y. Zeng, C.X. Ding, Microstructural characterization of plasma-sprayed nanostructured zirconia powders and coatings, Journal of the European Ceramic Society 23 (2003) 491–497.
[9] B. Ercan, K.J. Bowman, R.W. Trice, H. Wang, W. Porter, Effect of initial powder morphology on thermal and mechanical properties of stand-alone plasma-sprayed 7 wt% Y_2O_3–ZrO_2 coatings, Materials Science and Engineering A 435–436 (2006) 212–220.
[10] P. Roy, G. Bertrand, C. Coddet, Spray drying and sintering of zirconia based hollow powders, Powder Technology 157 (2005) 20–26.
[11] L. Wang, Y. Wang, X.G. Sun, J.Q. He, Z.Y. Pan, L.L. Yu, Preparation and characterization of nanostructured $La_2Zr_2O_7$ feedstock used for plasma spraying, Powder Technology 212 (2011) 267–277.
[12] J.R. Davis, Introduction to Thermal Spray Processing. Handbook of Thermal Technology, ASM International, USA, 2004, PP. 71–72.
[13] L. Wang, Y. Wang, X.G. Sun, J.Q. He, Z.Y. Pan, C.H. Wang, Microstructure and indentation mechanical properties of plasma sprayed nano-bimodal and conventional ZrO_2e8 wt%Y_2O_3 thermal barrier coatings, Vacuum 86 (2012) 1174–1185.
[14] L. Wang, Y. Wang, X.G. Sun, J.Q. He, Z.Y. Pan, C.H. Wang, A novel structure design towards extremely low thermal conductivity for thermal barrier coatings-experimental and mathematical study, Materials and Design 35 (2012) 505–517.
[15] X.C. Zhang, B.S. Xu, Y.X. Wu, F.Z. Xuan, S.T. Tu, Porosity, mechanical properties, residual stresses of supersonic plasma-sprayed Ni-based alloy coatings prepared at different powder feed rates, Applied Surface Science 254 (2008) 3879–3889.
[16] X.C. Zhang, B.S. Xu, S.T. Tu, F.Z. Xuan, H.D. Wang, Y.X. Wu, Effect of spraying power on the microstructure and mechanical properties of supersonic plasma-sprayed Ni-based alloy coatings, Applied Surface Science 254 (2008) 6318–6326.
[17] Z.H. Han, B.X. Xu, H.J. Wang, S.K. Zhou, A comparison of thermal shock behavior between currently plasma spray and supersonic plasma spray CeO_2–Y_2O_3–ZrO_2 graded thermal barrier coatings, Surface and Coatings Technology 201 (2007) 5253–5256.

[18] Y. Bai, Z.H. Han, H.Q. Li, C. Xu, Y.L. Xu, C.H. Ding, J.F. Yang, Structure–property differences between supersonic and conventional atmospheric plasma sprayed zirconia thermal barrier coatings, Surface and Coatings Technology 205 (2011) 3833–3839.
[19] J.C. Fang, W.J. Xu, Z.Y. Zhao, H.P. Zeng, In-flight behaviors of ZrO_2 particle in plasma spraying, Surface and Coatings Technology 201 (2007) 5671–5675.
[20] N.B. Keller, G. Bertrand, C. Filiatre, C. Meunier, C. Coddet, Microstructure of plasma-sprayed titania coatings deposited from spray-dried powder, Surface and Coatings Technology 168 (2003) 281–290.
[21] C.K. Lin, C.C. Berndt, Statistical analysis of microhardness variations in thermal spray coatings, Journal of Materials Science 30 (1995) 111–117.
[22] A. Dey, A.K. Mukhopadhyay, S. Gangadharan, M.K. Sinha, D. Basu, N.R. Bandyopadhyay, Nanoindentation study of microplasma sprayed hydroxyapatite coating, Ceramics International 35 (2009) 2295–2304.
[23] H. Zhou, F. Li, B. He, J. Wang, B.D. Sun, Air plasma sprayed thermal barrier coatings on titanium alloy substrates, Surface and Coatings Technology 201 (2007) 7360–7367.
[24] H.B. Xiong, L.L. Zheng, L. Li, A. Vaidya, Melting and oxidation behavior of in-flight particles in plasma spray process, International Journal of Heat and Mass Transfer 48 (2005) 5121–5133.
[25] H. Chen, C.X. Ding, Nanostructured zirconia coating prepared by atmospheric plasma spraying, Surface and Coatings Technology 150 (2002) 31–36.
[26] G.D. Girolamo, F. Marra, C. Blasi, E. Serra, T. Valente, Microstructure, mechanical properties and thermal shock resistance of plasma sprayed nanostructured zirconia coatings, Ceramics International 37 (2011) 2711–2717.
[27] R.S. Lima, A. Kucuk, C.C. Berndt, Integrity of nanostructured partially stabilized zirconia after plasma spray processing, Materials Science and Engineering A A 313 (2001) 75–82.
[28] L.L. Shaw, D. Goberman, R.M. Ren, M. Gell, S. Jiang, Y. Wang, T.D. Xiao, P.R. Strutt, The dependency of microstructure and properties of nanostructured coatings on plasma spray conditions, Surface and Coatings Technology 130 (2000) 1–8.
[29] Q.H. Yu, C.G. Zhou, H.Y. Zhang, F. Zhao, Thermal stability of nanostructured 13 wt% Al_2O_3–8 wt% Y_2O_3–ZrO_2 thermal barrier coatings, Journal of the European Ceramic Society 30 (2010) 889–897.
[30] R.S. Lima, A. Kucuk, C.C. Berndt, Bimodal distribution of mechanical properties on plasma sprayed nanostructured partially stabilized zirconia, Materials Science and Engineering A 327 (2002) 224–232.
[31] R.S. Lima, B.R. Marple, Y.S.Z. Nanostructured, Thermal barrier coatings engineered to counteract sintering effects, Materials Science and Engineering A 485 (2008) 182–193.